Journal Name

ARTICLE

Ionic Liquid Thin Layer-Induced Memory Effects in Organic Field-Effect Transistors

Received 00th January 20xx,
Accepted 00th January 20xx

DOI: 10.1039/x0xx00000x

www.rsc.org/

Keitaro Eguchi,*‡ Michio M. Matsushita, and Kunio Awaga*

We examined the morphologies and structures of pentacene and C_{60} thin films grown on thin layers of an ionic liquid, *N*,*N*-diethyl-*N*-methyl-*N*-(2-methoxyethyl)ammonium bis(trifluoromethanesulfonyl)imide (DEME–TFSI), and found that the characteristics of the films depended significantly on the thickness of DEME–TFSI. In addition, we fabricated organic field-effect transistors (OFETs) of pentacene and C_{60} in which a thin layer of DEME–TFSI was inserted between the organic semiconductor (pentacene or C_{60}) and the gate insulating layer, and measured their performance *in situ*. We found that 1.5~2 ML (ML: monolayer) DEME–TFSI produced a large hysteresis loop in the transfer characteristics in these OFETs, but 5 ML DEME–TFSI resulted in the formation of normally-on states with far smaller memory effects. The curvatures of the hysteresis loops were caused by the formation of trap states induced by the DEME–TFSI layers. This novel technique provides a simple tool for creating hysteresis behavior and could potentially be applied to transistor memory devices.

1. Introduction

Organic field-effect transistor (OFET) devices are key components used in organic electronics for the development of integrated circuits[1,2] and information storage devices.[3-5] In OFETs, charge carriers are induced in an organic semiconducting layer placed on a gate dielectric layer by the application of gate voltage, and they flow between the source and drain electrodes.[6,7] Ideally, the transfer characteristics of OFETs obtained by gate voltage sweep should not depend on the sweep direction. In many cases, however, the forward (off-to-on) and reverse (on-to-off) sweeps result in a hysteresis loop in the transfer characteristics due to the presence of carrier traps in the conductive channels between source and drain electrodes and/or at semiconductor-dielectric interfaces, as well as to the polarization and charging effects of dielectric layers.[8,9] Such a hysteresis loop is an unfavorable effect in switching devices, and dielectric materials, modified with self-assembled monolayers[10-12] and hydroxyl-free dielectric layers,[13,14] are used to diminish the hysteresis effects. However, hysteresis effects can be applied to memory devices, and various types of transistor memory devices, using ferroelectrics,[4,15] floating gate layers,[5,16 17] and charge-trapping dielectrics,[18,19] have been developed.

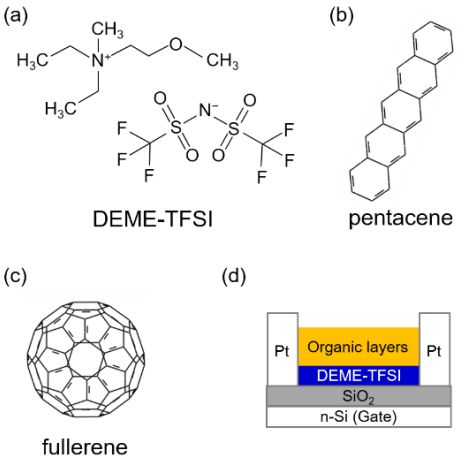

Figure 1. Chemical structures of (a) DEME–TFSI, (b) pentacene, and (c) C_{60}. (d) OFET device structure with DEME–TFSI layers.

Ionic liquids (ILs),[20,21] which consist of cations and anions, and hybrid materials between ILs and polymer materials[22,23] have been used as gate dielectric materials in OFETs to accumulate high-density carriers (~10^{15} cm^{-2}) in the semiconductor layers due to their high capacitances. This high-capacitance property originates in the mobile nature of cations and anions in ILs, resulting in the formation of electrical double layers (EDLs) at electrified solid-IL interfaces.[20,24,25] However, these properties are known to be significantly suppressed or modified when ILs are placed in confined conditions, such as the spaces in nanoporous materials,[26-29] due to the limitations of ion mobility. Using molecular dynamics simulations,

Department of Chemistry and Integrated Research Consortium on Chemical Science (IRCCS), Nagoya Univeristy, Furo-cho, Chikusa-ku, 464-8602 Nagoya, Japan.
E-mail: keitaro.eguchi@tum.de (KE), *awaga@mbox.chem.nagoya-u.ac.jp* (KA)
‡ Present address: *Physics Department, Technical University of Munich, James-Franck-Straße 1, D-85748 Garching, Germany*

† Electronic Supplementary Information (ESI) available: Schematic of an *in situ* measurement system, Topological and phase images of thin films of fullerene on 5 ML DEME–TFSI, Topological and phase images of DEME–TFSI on a thin film of pentacene (1.5 ML), Gate leakage current in transfer characteristics of the pentacene FETs; Extraction of parameters of μ_{FET}, ΔI, and ΔV_{th} from the transfer characteristics, Integrated values of $|I_{DS}(F)|$ and $|I_{DS}(R)|$ and their differences; Transfer characteristics of (a) pentacene (IL: 2 ML) and (b) C_{60} (IL: 1.5 ML) devices for three cycles;Transfer characteristics of the pentacene and fullerene FETs with the DEME-TFSI layers measured at different V_{DS}. See DOI: 10.1039/x0xx00000x

Please do not adjust margins

Feng and Cummings found that the spatial distribution of ions accumulated in confined pores depends strongly on pore size (ranging from 0.7 to 1.6 nm).[28] Futamura *et al*. reported unique mono- and bi-layer structures of 1-ethyl-3-methylimidazolium bis(trifluoromethylsulfonyl)imide (EMIM–TFSI) in the confined spaces of carbon nanopores with diameters of 0.7 and 1 nm, respectively.[29] From this perspective, it is expected that, if a thin IL layer is inserted into a confined space between an organic semiconductor and a dielectric material in an OFET, the immobile charges of cations and/or anions of the IL would electrostatically interact with the carriers induced in the semiconductor layer and act as carrier trap sites. This would probably create a hysteresis loop in the transfer characteristics,[9] which would be controllable by the thickness of the IL layer.

In the present work, we used *ex situ* atomic force microscopy (AFM) and X-ray diffraction (XRD) to examine the morphology and structure of thin layers of an IL, *N*,*N*-diethyl-*N*-methyl-*N*-(2-methoxyethyl)ammonium bis(trifluoromethanesulfonyl)imide (DEME–TFSI, Figure 1a), as well as of thin films of pentacene (Figure 1b) and C_{60} (Figure 1c) deposited on DEME–TFSI thin layers. Moreover, we fabricated OFETs under a high vacuum by inserting a thin layer of DEME–TFSI between an organic semiconductor and SiO_2 gate dielectrics (Figure 1d), and then performed *in situ* FET measurements without exposure to air. As p- and n-types organic semiconductors, we used pentacene and C_{60}, respectively, because they are sublimable and thin films of them are well-characterized and exhibit relatively high mobilities.[10,30,31] Finally, we discuss the IL thin layer-induced memory effects in the transfer characteristics of the OFETs.

2. Results and Discussion

Thin layers of DEME–TFSI were thermally deposited on Si substrates having thermally oxidized surfaces (300 nm) under a high vacuum. Figure 2a–c show AFM images of the DEME–TFSI layers with thicknesses of D = 0, 1, and 5 ML (ML: monolayer), respectively, where 1 ML corresponds to 0.78 pairs of $DEME^+$ and $TFSI^-$ per nm^2 unit.[32] AlthoughThe surface morphology of the bare SiO_2/Si substrate (D = 0 ML) is flat, and the height difference is estimated to be 0.54 nm from the cross-sectional profile (broken line AB). The surface morphology of the D = 1 ML sample (Figure 2b) is still flat without any aggregation. The height difference on the broken-line CD is 0.60 nm, which is comparable to that of the bare SiO_2/Si substrate. At D = 5 ML (Figure 2c), the AFM image is completely different from those at D = 0 and 1 ML; 5 ML DEME–TFSI forms islands with a height of ~4 nm.

Immediately after producing the above thin layers of DEME–TFSI, we grew thin films of pentacene (10 ML) or C_{60} (20 ML) on them while maintaining the high vacuum condition (see Figure 1d and S1). Figure 2d–f show AFM images of the pentacene thin films on the DEME–TFSI layers with thicknesses of D = 0, 1, and 5 ML, respectively. The film without a DEME–TFSI layer (D = 0 ML), which was prepared

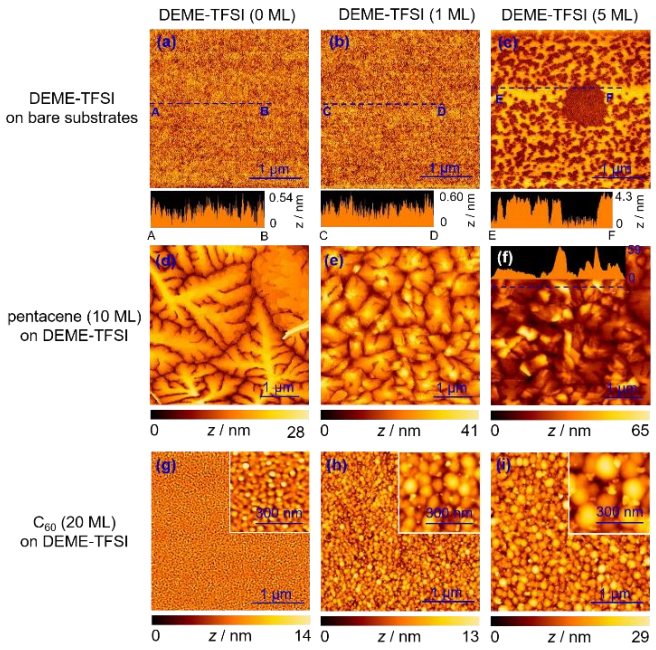

Figure 2. AFM images of (a–c) DEME–TFSI layers prepared on bare substrates, (d–f) pentacene (10 ML), and (g–i) C_{60} (20 ML) thin films prepared on (d,g) 0 ML, (e,h) 1 ML, and (f,i) 5 ML DEME–TFSI. The sizes of the AFM images are 3 μm × 3 μm for (a-c, g-i) and 4 μm × 4 μm for (d-f). In panels (g–i), the insets show magnified images. In panels (a–c, f), cross-sectional profiles on the dashed blue lines are also shown together.

on bare SiO_2/Si substrate, exhibits a dendritic structure several micrometers in size (Figure 2d). This feature agrees with the data reported previously.[30,33] The pentacene thin film on the 1 ML DEME–TFSI also exhibits a dendritic structure (Figure 2e), but the domain sizes in this film are much smaller than those in the film in Figure 2d. Since the surface morphology of the 1 ML DEME–TFSI on the SiO_2/Si substrate is nearly the same as that of the bare SiO_2/Si substrate (see Figure 2a and 2b), the smaller domains of the pentacene on the 1 ML DEME–TFSI would be caused by the short surface diffusion length of the adsorbed pentacene on the IL.[30,34] Figure 2f shows an AFM image of the pentacene thin film prepared on the 5 ML DEME–TFSI. It is very different from those of the films prepared on 0 and 1 ML DEME–TFSI shown in Figure 2d and 2e, respectively. The image in Figure 2f consists of dark and bright parts; the former shows thin, dendritic grains while the latter shows thick, nondendritic grains. This feature is attributed to the surface morphology of the 5 ML DEME–TFSI, which has coexisting aggregated and nonaggregated DEME–TFSI domains (Figure 2c). It is considered that the dendritic and nondendritic structures of pentacene would form on the nonaggregated and aggregated domains of DEME–TFSI, respectively, because the growth of pentacene on the nonaggregated DEME–TFSI domain should be similar to that on the 1 ML DEME–TFSI.

The thin films of pentacene were also examined by XRD, revealing their molecular ordering and packing. The black curve in Figure 3a shows the results for the pentacene thin film without a DEME–TFSI layer, indicating a sharp diffraction peak at 2ϑ = 5.7° with a weak satellite peak at 5.2°, along with higher-order peaks at 11.4,

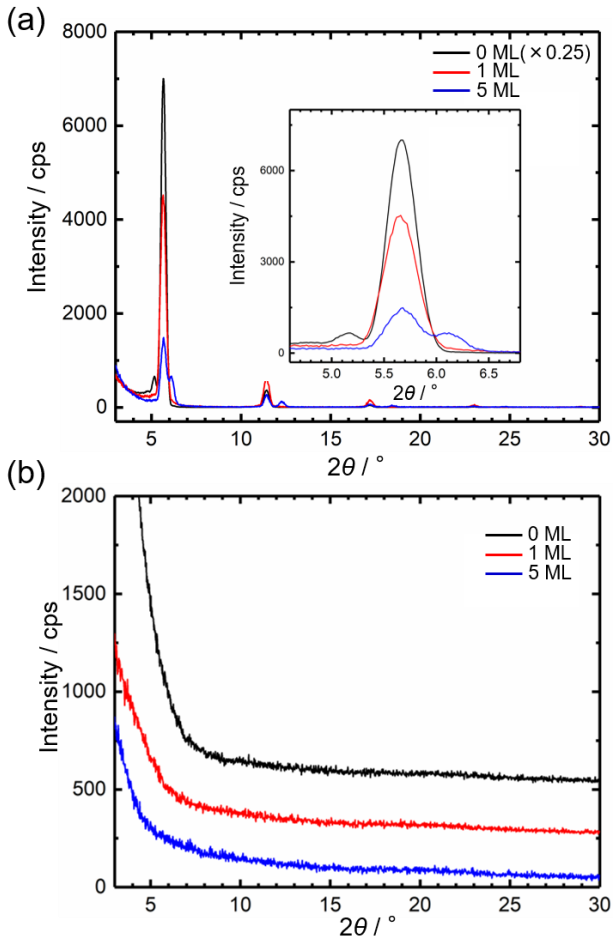

Figure 3. XRD patterns of (a) pentacene and (b) C_{60} thin films prepared on 0 ML (black), 1 ML (red), and 5 ML (blue) DEME–TFSI. The inset in panel (a) shows a magnified view of the XRD peaks in the dashed-line region of the main pattern. In panel (b), offsets of 500 and 250 cps in intensity were added to 0 ML (black) and 1 ML (red), respectively.

17.2, 23.0, and 28.8°. The first-order diffraction peak corresponds to the diffraction from the (001) plane of the thin-film phase of pentacene on SiO_2 with an interplanar spacing of d = 15.5 Å. This agrees with the results of previous reports.[35-37] The red curve in Figure 3a shows the XRD for the pentacene thin films prepared on the DEME–TFSI layer of D = 1 ML. It also exhibits a series of diffraction peaks of d = 15.5 Å, but their intensities are significantly lower than those for the D = 0 ML sample and there is no satellite peak. The blue curve in Figure 3a shows the XRD for the pentacene thin film grown on the 5 ML DEME–TFSI. Besides the diffraction series of 2ϑ = 5.7°, this curve indicates another periodicity with the first- and second-order diffractions at 2ϑ = 6.1° and 12.2°, respectively. These diffractions indicate an interplanar distance of d = 14.5 Å. This value agrees with that for the (001) plane in the bulk pentacene phase found in its single crystals[38] and thin films.[35,36] This means that the pentacene thin films on 5 ML DEME–TFSI include both the thin-film and bulk phases of pentacene. It is known that pentacene thermally deposited into droplets of ILs forms the bulk phase,[39] so that the bulk phase of pentacene is considered to grow in the aggregations of DEME–TFSI found for the 5 ML thin films (see Figure 2c). These XRD data for the 5 ML sample are consistent with the results of the AFM measurements, which reveal two domains: thin, dendritic grains and thick, nondendritic ones. It is reasonable to infer that the former and the latter are the thin-film and bulk phases of pentacene, respectively.

The morphologies and structures of the thin films of C_{60} were also examined with and without a DEME–TFSI layer. Figure 2g–i show AFM images of the thin films of C_{60} prepared on 0, 1, and 5 ML of DEME–TFSI on the SiO_2/Si substrates, respectively. The grain sizes in these thin films increase in this order; the grain diameters on the 0, 1, and 5 ML DEME–TFSI are 40, 80, and 150 nm, respectively. This means that the DEME–TFSI layers promote the growth of C_{60} grains. In the images of the latter two films formed on 1 and 5 ML DEME–TFSI, very small bright particles (10~20 nm) can also be seen around the large grains. Figure S2 shows a topological AFM image and a corresponding phase image of a fullerene thin film (20 ML) prepared on 5 ML DEME–TFSI. This phase image clearly indicates that these small particles consist of a different material from that of the large grains. The height and area of the large grains, shown in Figure S2, suggest that these grains are made of C_{60}, and the small dots are presumably made of DEME–TFSI. It is notable that, although such small dots of DEME–TFSI are not seen in the images for the pentacene thin films (Figure 2d-f), they appear when DEME–TFSI is deposited on a thin film of pentacene (see Figure S3). No thin films of C_{60} exhibit diffraction peaks in the XRD spectra, as shown in Figure 3b, suggesting the poor crystallinity of C_{60} grains.

To investigate the effects on FET characteristics of a thin layer of IL between an organic semiconductor and a gate insulator, we deposited DEME–TFSI on a bottom-gate FET substrate with an SiO_2 insulating layer (300 nm) and then deposited thin films of pentacene (10 ML) or C_{60} (20 ML) on DEME–TFSI without exposure to air. We then carried out *in situ* FET measurements under high vacuum conditions. The details are described in the Experimental Section (see also Figure 1d and S1). Figure 4a shows the transfer characteristics of pentacene FETs including DEME–TFSI layers with thicknesses of 0, 1, 2, and 5 ML. The same data are shown in Figure 4b on an enlarged scale. These data were collected at a fixed source-drain voltage V_{DS} of –20 V at intervals of 0.3 s with a step of 2 V. In these devices, the gate leakage currents were on the order of 1×10^{-7} A (Figure S4). The black curve in Figure 4 shows the results for the FET without a DEME–TFSI layer, indicating typical p-type behavior with a small hysteresis loop. This agrees with a previous result.[12] The small hysteresis is caused by the presence of interfacial traps.[9] The red and green curves in this figure show the data for the devices including 1 and 2 ML DEME–TFSI, respectively. Compared with the black curve for the 0 ML device, the red curve in the forward sweep exhibits a significant positive shift in the threshold voltage and a gradual increase in $|I_{DS}|$. The value of $|I_{DS}|$ at −130 V is 6 times smaller than that for the 0 ML device. In addition, the reverse sweep in the red curve indicates a faster decrease in $|I_{DS}|$ than the increase in the forward sweep, resulting in hysteresis. The positive shift of the

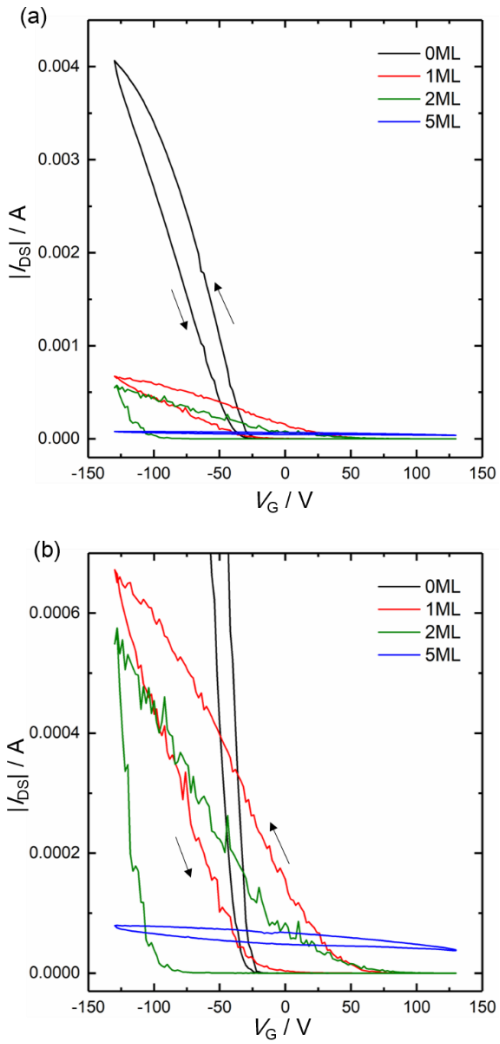

Figure 4. Transfer characteristics of 10 ML pentacene FETs without DEME–TFSI (black) and with 1 ML (red), 2 ML (green), and 5 ML DEME–TFSI (blue), measured at V_{DS} = –20 V in the dark. (a) Overall view and (b) magnified view around the 1 ML device. The arrows represent the sweep directions. The inset in the panel shows a whole view of the transfer characteristics.

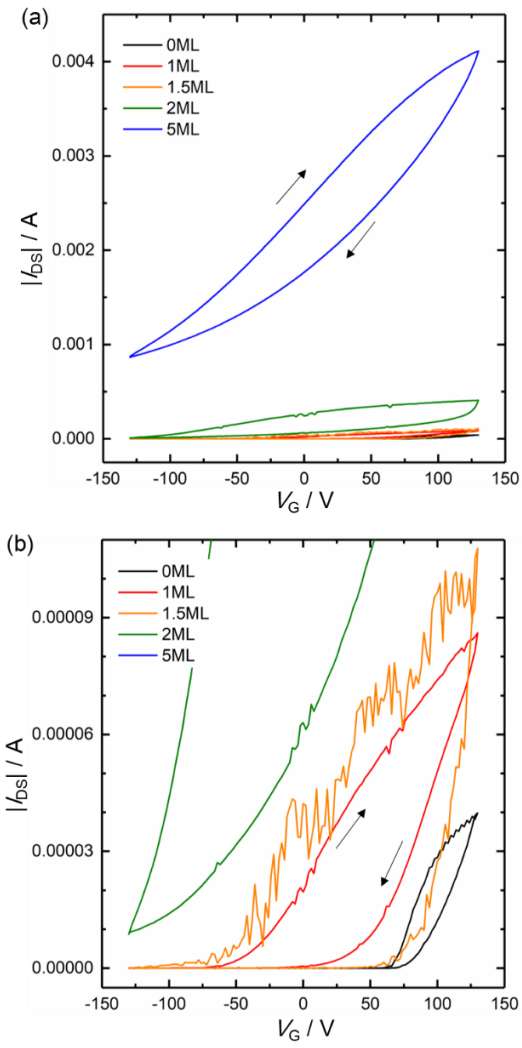

Figure 5. Transfer characteristics of 20 ML C60 FETs with 0 ML (black), 1 ML (red), 1.5 ML (orange), 2 ML (green), and 5 ML DEME–TFSI (blue), measured at VDS = +20 V in the dark. (a) Overall view and (b) magnified view around the 1 ML device. The arrows represent the sweep directions. The inset in the panel shows a whole view of the transfer characteristics.

threshold voltage is probably caused by a built-in potential produced by the dipoles in DEME–TFSI and/or by the intermolecular interactions between DEME–TFSI and pentacene, as reported for OFETs with self-assembled monolayers.[12, 40] The green curve for the 2 ML device also exhibits a hysteresis loop, which is larger than that for the 1 ML DEME–TFSI device. Comparison between the red and green curves suggests an interesting relation: the increase in $|I_{DS}|$ in the forward sweep is faster for the red curve, but the decrease in $|I_{DS}|$ in the reverse sweep is faster for the 2 ML device. This suggests that the hysteresis is caused by the formation of DEME–TFSI-induced trapping sites in the pentacene layer. It is expected that the presence of the traps would decrease the speed of the initial increase in $|I_{DS}|$ in the forward sweep, because the injected carriers are trapped or scattered by the traps. On the other hand, the filled traps would not affect the speed of the initial decrease in $|I_{DS}|$ in the reverse sweep, because this decay is caused by a simple decrease in the carrier density. The difference between the 1 ML (red curve) and 2 ML (green curve) devices can be explained by an increase in the trap number in the latter. Although it is reported that the pentacene film can change its crystalline phase when it is charged,[41] we believe that the hysteresis behaviour in the present research is mainly caused by the presence of the ionic liquid layers because the hysteresis width found in this study is much larger than that reported in the above reference. It is worth noting the noisy feature of both the red and green curves in Figure 4, which always appears in multiple measurements and even in other devices. This is presumably caused by the trapping and detrapping of the charge carriers. The blue curve in Figure 4 shows the data for the 5 ML DEME–TFSI device, on which the dependence of $|I_{DS}|$ on V_G disappears, and the values of $|I_{DS}|$ are much larger than those of the off states in the other devices. This is attributable to the significant increase in the carrier number, which prevents the formation of the off state. It is seen that the values of

Table 1. The field-effect mobility (μ_{FET}), memory-ratio (I_F/I_R), and memory-window (ΔV_{th}) parameters extracted from the transfer characteristics. The number of trapped carriers was estimated from the values of ΔV_{th} using equation (1). F and R are the forward and reverse sweeping directions, respectively.

	$D_{DEME-TFSI}$	μ_{FET} / cm^2 (Vs)$^{-1}$	I_F/I_R at $V_G = 0$	ΔV_{th} / V	Δn / cm^{-2}
Pentacene	0 ML	(F) 0.71, (R) 0.58	~1	1.1×10^1	7.8×10^{11}
	1 ML	(F) 0.066, (R) 0.082	4.9×10^2	5.9×10^1	4.2×10^{12}
	2 ML	(F) 0.052, (R) 0.35	1.2×10^3	1.2×10^2	8.4×10^{12}
	5 ML	–	1.4	–	–
C_{60}	0 ML	(F) 0.013, (R) 0.011	~1	2.4×10^1	1.7×10^{12}
	1 ML	(F) 0.0075, (R) 0.013	4.0×10^1	9.3×10^1	6.8×10^{12}
	1.5 ML	(F) 0.0072, (R) 0.022	1.1×10^3	1.5×10^2	1.1×10^{13}
	2 ML	–	3.9	–	–
	5 ML	–	1.4	–	–

$|I_{DS}|$ at V_G = –130 V decrease as the thickness of DEME–TFSI increases. This can be explained by the significant decrease in FET mobility, as discussed later (Table 1).

Figure 5a,b show an overall view and a magnified view, respectively, of the transfer characteristics of the C_{60} FETs with DEME–TFSI layers of 0, 1, 1.5, 2, and 5 ML. They were measured at V_{DS} = +20 V, and the other measurement conditions were the same as those used for the pentacene FETs. The black curve in Figure 5 shows the results for the C_{60} FET without the DEME–TFSI layer, indicating a typical n-type behavior with a small hysteresis loop. This feature agrees with the data in the literature.[10] The red and orange curves in this figure show the results for the devices with 1 and 1.5 ML DEME–TFSI, respectively. Compared with the black curve for the 0 ML device, the red and orange curves in the forward sweep exhibit significant negative shifts of threshold voltage and large hysteresis loops in $|I_{DS}|$. These results can be explained by the same mechanism discussed above for the pentacene FETs. The green and blue curves in Figure 5 show the data for the 2 and 5 ML devices, respectively. Their $|I_{DS}|$ are much larger than the off-state current in the other three devices, as found for the pentacene FET with 5 ML DEME–TFSI. It is notable that the on-state current, namely $|I_{DS}|$ at V_G = 130 V, in the C_{60} FETs increases with increasing thickness of DEME–TFSI. Because there is no significant change in mobility for the C_{60} FETs, as shown later (Table 1), the increase in $|I_{DS}|$ at V_G = 130 V would be explained by the negative shift of V_{th}, which increases the carrier density. It is notable that the effects of the DEME–TFSI layers on the on-state currents in the pentacene and C_{60} FETs are completely opposite. This is probably caused by the differences in crystallinity and mobility between the pentacene and C_{60} FETs; the band-like transport in the pentacene films with high crystallinity would be easily spoiled by the perturbations from the DEME–TFSI layers, while the hopping-like transport in the C_{60} films with low crystallinity would not be.

The field-effect mobility (μ_{FET}), the I_{DS} ratio in the forward and reverse sweeps at V_G = 0 V (I_F/I_R), and the voltage shift in the threshold voltage (ΔV_{th}) were calculated from the transfer characteristics of the pentacene and C_{60} FETs, as shown in Figure 4 and 5, respectively. The definitions of I_F/I_R and ΔV_{th} are shown in Figure S5. The obtained values are listed in Table 1. The values of I_F/I_R and ΔV_{th} depend strongly on the thicknesses of the DEME–TFSI layers. The insertion of 1.5~2 ML DEME–TFSI to the pentacene and C_{60} FETs significantly enhances I_F/I_R by ~10^3 compared with the corresponding data for the 0 ML devices. However, the values of I_F/I_R decrease significantly, to ~1.4 for the 5 ML DEME–TFSI for both devices. The ΔV_{th} values also increase, to 1.2×10^2 and 1.5×10^2 V for the 2 ML DEME–TFSI pentacene and the 1.5 ML DEME–TFSI C_{60} FETs, respectively. From the obtained ΔV_{th} values, we estimated the number of trapped carriers (Δn) using the following equation:

$$\Delta n = (C_i \times \Delta V_{th})/e \,. \quad (1)$$

Here, C_i is the capacitance per unit area of the SiO_2 insulating layer and e is the elementary charge. The results are also shown in Table 1, indicating that the insertion of the DEME–TFSI layer significantly increases the trapped carriers. When the thickness of DEME–TFSI is 1 ML, the carrier-trapping efficiencies $\eta = \Delta n / \rho$, where ρ is the density of DEME–TFSI per unit area, are calculated to be 5.4% and 8.7% for the pentacene and C_{60} devices, respectively. This suggests that the carrier trapping can be controlled by tuning the thickness of the DEME–TFSI layer. We also calculated the effective area of the hysteresis loops (ES) using the following equation:

$$ES = \frac{\left\{\int_{-130}^{+130} |I_{DS}(F)|\, dV - \int_{-130}^{+130} |I_{DS}(R)|\, dV\right\}}{\int_{-130}^{+130} |I_{DS}(F)|\, dV} \,. \quad (2)$$

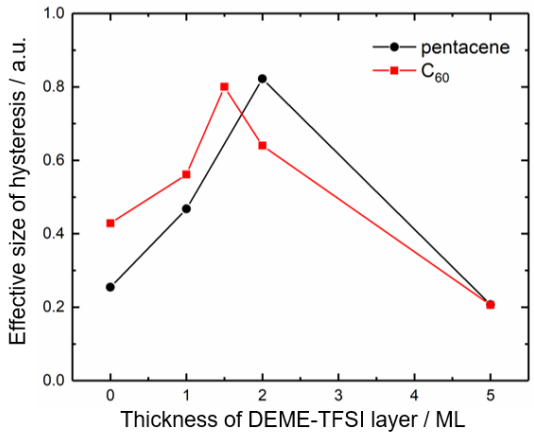

Figure 6. Effective size of hysteresis calculated using equation (2) in the text.

Here, $|I_{DS}(F)|$ and $|I_{DS}(R)|$ represent $|I_{DS}|$ in the forward and reverse sweeps, respectively. The values of $\int_{-130}^{+130}|I_{DS}(F)|\,dV$, $\int_{-130}^{+130}|I_{DS}(R)|\,dV$, and their differences, $\int_{-130}^{+130}|I_{DS}(F)|\,dV - \int_{-130}^{+130}|I_{DS}(R)|\,dV$, are shown in Figure S6, and the calculated *ES* values are presented in Figure 6. The *ES* values for the pentacene and C_{60} OFETs depend on the thickness of DEME–TFSI, reaching a maximum around 1.5~2 ML. This means that the memory effects in the transfer characteristics are maximized in that range.

3. Conclusions

We investigated the memory effects of OFETs induced by the insertion of DEME–TFSI thin layers between an organic semiconductor and a gate insulator. We found that the transistor performance depended significantly on the thickness of the IL layer, and that both the pentacene and C_{60} OFETs exhibited large hysteresis loops in the thickness range of 1.5~2 ML. However, the insertion of 5 ML DEME–TFSI resulted in the formation of normally-on states in both films, while the on-currents were significantly suppressed and enhanced in the pentacene and C_{60} devices, respectively.

4. Experimental methods

Pentacene (Tokyo Chemical Industry) and C_{60} (Sigma-Aldrich) were purified by thermal-gradient sublimation with continuous N_2 gas flows (~40 or 60 ml min^{-1}). DEME–TFSI (Kanto Chemical) was used without further purification. Through the present research, it was stored in a high vacuum to prevent contamination. Preparations of thin films and *in situ* FET measurements were performed using a homemade high vacuum chamber.[42,43] Pentacene, C_{60}, and DEME–TFSI were individually mounted in deposition cells. Prior to deposition, they were degassed in a high vacuum chamber (base pressure of 5×10^{-5} Pa). DEME–TFSI was deposited at a rate of ~0.2 ML min^{-1} at room temperature on the FET substrates with a bottom-gate bottom-contact-device architecture with SiO_2 insulating layers (300 nm) thermally grown on highly doped n-Si substrates (gate electrodes) and comb-shaped Pt electrodes (width/length = 7.9 cm/20 μm). Subsequently, thin films of pentacene (10 ML) and C_{60} (20 ML) were prepared on the substrates without exposure to air. The deposition rates were controlled at ~0.2 ML min^{-1} for DEME–TFSI and pentacene and at ~0.4 ML min^{-1} for C_{60} using a quartz crystal microbalance. During the depositions, no electrical voltage was applied to the source, drain, or gate electrodes. FET measurements were performed *in situ* under high vacuum conditions without exposure to air at room temperature in the dark, using a source-measure unit (Advantest Corp. R6245A). V_{DS} values of –20 and +20 V were applied in the operations for the thin films of pentacene and C_{60} FETs, respectively. The V_G was scanned between +130 and –130 V. No significant reduction in I_{DS} of the transfer characteristics was observed during the operations (see Figure S7). The transfer characteristics measured at different V_{DS} values of –30, –10, 0, +10, or +30 V are shown in Figure S8, which indicates that the devices were operated in linear regimes.

Ex situ structural and morphological characterization using XRD (Rigaku Smart Lab X-ray diffractometer) and AFM (Seiko Instruments SPI 3800/SPA400) under ambient conditions were performed for the thin films at room temperature. The XRD signals were recorded using Cu Kα radiation (40 kV, 40 mA) operated in the ϑ–2ϑ mode. The AFM images were obtained in dynamic-force mode using a Si tip. The samples for these measurements were prepared on Si substrates with thermally oxidized surfaces (300 nm) under the same conditions used to prepare the FET devices. Although bulk DEME–TFSI is liquid at room temperature, there was no technical difficulty on the AFM measurements because of its solid-like behaviour on substrate surfaces.[32,44,45]

Acknowledgements

This study was supported by Japan Society for the Promotion of Science (JSPS) KAKENHI Grants (nos. JP16H06353 and JP18H04482) and by the JSPS Bilateral Collaboration. We also acknowledge a research grant from The Murata Science Foundation.

References

1. B. Crone, A. Dodabalapur, Y. Y. Lin, R. W. Filas, Z. Bao, A. LaDuca, R. Sarpeshkar, H. E. Katz, W. Li, *Nature* **2000**, 403, 521.
2. M. Kaltenbrunner, T. Sekitani, J. Reeder, T. Yokota, K. Kuribara, T. Tokuhara, M. Drack, R. Schwödiauer, I. Graz, S. Bauer-Gogonea, S. Bauer, T. Someya, *Nature* **2013**, 499, 458.
3. S. T. Han, Y. Zhou, V. A. L. Roy, *Adv. Mater.* **2013**, 25, 5425.
4. R. Schroeder, L. A. Majewski, M. Grell, *Adv. Mater.* **2004**, 16, 633.
5. T. Sekitani, T. Yokota, U. Zschieschang, H. Klauk, S. Bauer, K. Takeuchi, M. Takamiya, T. Sakurai, T. Someya, *Science* **2009**, 326, 1516.
6. G. Horowitz, *J. Mater. Res.* **2004**, 19, 1946.
7. H. Klauk, *Chem. Soc. Rev.* **2010**, 39, 2643.

8. D. K. Hwang, M. S. Oh, J. M. Hwang, J. H. Kim, S. Im, *Appl. Phys. Lett.* **2008**, 92, 013304.
9. M. Egginger, S. Bauer, R. Schwödiauer, H. Neugebauer, N. S. Sariciftci, *Monatsh. Chem.* **2009**, 140, 735.
10. M. Kitamura, Y. Kuzumoto, M. Kamura, S. Aomori, Y. Arakawa, *Appl. Phys. Lett.* **2007**, 91, 183514.
11. E. C. P. Smits, S. G. J. Mathijssen, P. A. van Hal, S. Setayesh, T. C. T. Geuns, K. A. H. A. Mutsaers, E. Cantatore, H. J. Wondergem, O. Werzer, R. Resel, M. Kemerink, S. Kirchmeyer, A. M. Muzafarov, S. A. Ponomarenko, B. de Boer, P. W. M. Blom, D. M. de Leeuw, *Nature* **2008**, 455, 956.
12. M.-H. Yoon, C. Kim, A. Facchetti, T. J. Marks, *J. Am. Chem. Soc.* **2006**, 128, 12851.
13. J. Jang, S. H. Kim, S. Nam, D. S. Chung, C. Yang, W. M. Yun, C. E. Park, J. B. Koo, *Appl. Phys. Lett.* **2008**, 92, 143306.
14. M. P. Walser, W. L. Kalb, T. Mathis, B. Batlogg, *Appl. Phys. Lett.* **2009**, 95, 233301.
15. R. Schroeder, L. A. Majewski, M. Voigt, M. Grell, *IEEE Electr. Device L.* **2005**, 26, 69.
16. T. Itoh, T. Toyota, H. Higuchi, M. M. Matsushita, K. Suzuki, T. Sugawara, *Chem. Phys. Lett.* **2017**, 671, 71.
17. H. C. Chang, C. Lu, C. L. Liu, W. C. Chen, *Adv. Mater.* **2015**, 27, 27.
18. T. D. Tsai, J. W. Chang, T. C. Wen, T. F. Guo, *Adv. Funct. Mater.* **2013**, 23, 4206.
19. K.-J. Baeg, Y.-Y. Noh, J. Ghim, S.-J. Kang, H. Lee, D.-Y. Kim, *Adv. Mater.* **2006**, 18, 3179.
20. T. Fujimoto, K. Awaga, *Phys. Chem. Chem. Phys.* **2013**, 15, 8983.
21. S. Z. Bisri, S. Shimizu, M. Nakano, Y. Iwasa, *Adv. Mater.* **2017**, 29.
22. J. Lee, M. J. Panzer, Y. He, T. P. Lodge, C. D. Frisbie, *J. Am. Chem. Soc.* **2007**, 129, 4532.
23. K. H. Lee, M. S. Kang, S. Zhang, Y. Gu, T. P. Lodge, C. D. Frisbie, *Adv. Mater.* **2012**, 24, 4457.
24. D. T. Limmer, *Phys. Rev. Lett.* **2015**, 115, 256102.
25. S. Baldelli, *J. Phys. Chem. Lett.* **2013**, 4, 244.
26. C. Largeot, C. Portet, J. Chmiola, P.-L. Taberna, Y. Gogotsi, P. Simon, *J. Am. Chem. Soc.* **2008**, 130, 2730.
27. S. Kondrat, A. Kornyshev, *J. Phys.: Condens. Matter.* **2013**, 25, 119501.
28. G. Feng, P. T. Cummings, *J. Phys. Chem. Lett.* **2011**, 2, 2859.
29. R. Futamura, T. Iiyama, Y. Takasaki, Y. Gogotsi, M. J. Biggs, M. Salanne, J. Ségalini, P. Simon, K. Kaneko, *Nat. Mater.* **2017**, 16, 1225.
30. R. Ruiz, D. Choudhary, B. Nickel, T. Toccoli, K.-C. Chang, A. C. Mayer, P. Clancy, J. M. Blakely, R. L. Headrick, S. Iannotta, G. G. Malliaras, *Chem. Mater.* **2004**, 16, 4497.
31. T. D. Anthopoulos, B. Singh, N. Maranovic, N. S. Sariciftci, A. M. Ramil, H. Sitter, M. Cölle, D. M. de Leeuw, *Appl. Phys. Lett.* **2006**, 89, 213504.
32. F. Buchner, K. Forster-Tonigold, M. Bozorgchenani, A. Gross, R. J. Behm, *J. Phys. Chem. Lett.* **2016**, 7, 226.
33. A. Shehu, S. D. Quiroga, P. D'Angelo, C. Albonetti, F. Borgatti, M. Murgia, A. Scorzoni, P. Stoliar, F. Biscarini, *Phys. Rev. Lett.* **2010**, 104, 246602.
34. J. G. Amar, F. Family, P.-M. Lam, *Phys. Rev. B* **1994**, 50, 8781.
35. D. Knipp, R. A. Street, A. Völkel, J. Ho, *J. Appl. Phys.* **2003**, 93, 347.
36. C. D. Dimitrakopoulos, A. R. Brown, A. Pomp, *J. Appl. Phys.* **1996**, 80, 2501.
37. S. Schiefer, M. Huth, A. Dobrinevski, B. Nickel, *J. Am. Chem. Soc.* **2007**, 129, 10316.
38. R. B. Campbell, J. M. Robertson, J. Trotter, *Acta Crystallogr.* **1961**, 14, 705.
39. Y. Takeyama, S. Maruyama, Y. Matsumoto, *Cryst. Growth Des.* **2011**, 11, 2273.
40. S. Kobayashi, T. Nishikawa, T. Takenobu, S. Mori, T. Shimoda, T. Mitani, H. Shimotani, N. Yoshimoto, S. Ogawa, Y. Iwasa, *Nat. Mater.* **2004**, 3, 317.
41. M. Ando, T. B. Kehoe, M. Yoneya, H. Ishii, M. Kawasaki, C. M. Duffy, T. Minakata, R. T. Phillips, H. Sirringhaus, *Adv. Mater.* **2015**, 27, 122.
42. K. Eguchi, M. M. Matsushita, K. Awaga, *J. Phys. Chem. C* **2018**, 122, 26054.
43. K. Eguchi, Y. Imai, M. M. Matsushita, K. Awaga, *J. Phys. Chem. C* **2018**, 122, 7731.
44. B. Uhl, T. Cremer, M. Roos, F. Maier, H.-P Steinruck, R. J. Behm, *Phys. Chem. Chem. Phys.* **2013**, 15, 17295.
45. B. Uhl, M. Hekmatfar, F. Buchner, R. J. Behm, *Phys. Chem. Chem. Phys.* **2016**, 18, 6618.